Check for updates

NANO · MICRO small
www.small-journal.com

Ionic Conductive and Highly-Stable Interface for Alkali Metal Anodes

Enzhong Jin, Karnpiwat Tantratian, Changtai Zhao, Anastasia Codirenzi, Lyudmila V. Goncharova, Changhong Wang, Feipeng Yang, Yijia Wang, Parham Pirayesh, Jinghua Guo, Lei Chen, Xueliang Sun,* and Yang Zhao**

Alkali metals are regarded as the most promising candidates for advanced anode for the next-generation batteries due to their high specific capacity, low electrochemical potential, and lightweight. However, critical problems of the alkali metal anodes, especially dendrite formation and interface stabilization, remain challenging to overcome. The solid electrolyte interphase (SEI) is a key factor affecting Li and Na deposition behavior and electrochemical performances. Herein, a facile and universal approach is successfully developed to fabricate ionic conductive interfaces for Li and Na metal anodes by modified atomic layer deposition (ALD). In this process, the Li metal (or Na metal) plays the role of Li (or Na) source without any additional Li (or Na) precursor during ALD. Moreover, the key questions about the influence of ALD deposition temperature on the compositions and structure of the coatings are addressed. The optimized ionic conductive coatings have significantly improved the electrochemical performances. In addition, the electrochemical phase-field model is performed to prove that the ionic conductive coating is very effective in promoting uniform electrodeposition. This approach is universal and can be potentially applied to other different metal anodes. At the same time, it can be extended to other types of coatings or other deposition techniques.

1. Introduction

Alkali metal anodes, such as Li and Na metals, with high theoretical capacity, low electrochemical potential, and lightweight, are considered as the most promising candidates for the next-generation alkali-metal batteries, including Li/Na-S, Li/Na-O_2, and all-solid-state Li/Na metal batteries.[1] However, several serious challenges exist for alkali metal anodes, limiting their practical applications. The dendrite growth is one of the major challenges, which leads to undesired safety concerns, low Coulombic efficiency (CE) and inactive "dead Li/Na" layer formation.[2] The solid electrolyte interphase (SEI) layer, naturally formed due to the chemical/electrochemical reaction between alkali metal and electrolyte, is critical for the electrochemical deposition behavior and electrochemical performances of the alkali metal anode, in which the structure, composition, and stability of the SEI layer are key factors.[3] An unstable SEI layer can promote dendrite growth due to nonuniform ion flux distribution and nonhomogeneous alkali metal deposition, leading to large polarization and decay of the electrochemical performances.[4] Tremendous efforts have been attempted to stabilize the SEI via different approaches, including modifying the electrolyte components and creating artificial SEI layers for alkali metal anode. The artificial SEI layers are expected to block the side reactions between electrolyte and alkali metal, stabilize the interface, reduce the dendrite growth, and improve performance.[5] Many protective layers have been developed for both Li and Na metal anodes, including inorganic layers, organic layers, and organic–inorganic hybrid layers.[6]

Generally, an ideal artificial SEI layer should possess the properties of ultrathin thickness, uniform and complete

E. Jin, C. Zhao, C. Wang, Y. Wang, P. Pirayesh, X. Sun, Y. Zhao
Department of Mechanical and Materials Engineering
University of Western Ontario
London, ON N6A 5B9, Canada
E-mail: xsun9@uwo.ca; yzhao628@uwo.ca

K. Tantratian, L. Chen
Department of Mechanical Engineering
University of Michigan–Dearborn
Dearborn, MI 48128, USA
E-mail: leichn@umich.edu

The ORCID identification number(s) for the author(s) of this article can be found under https://doi.org/10.1002/smll.202203045.

A. Codirenzi, L. V. Goncharova
Department of Physics and Astronomy
University of Western Ontario
London, ON N6A 3K7, Canada

F. Yang, J. Guo
Advanced Light Source
Lawrence Berkeley National Laboratory
Berkeley, CA 94720, USA

L. Chen
Michigan Institute for Data Science
University of Michigan
Ann Arbor, MI 48109, USA

DOI: 10.1002/smll.202203045

© 2022 Wiley-VCH GmbH

coating, high ionic conductivity, sufficient density, and good mechanical stability. The fabrication of an ideal artificial SEI layer that can meet all these requirements is a challenge. Atomic layer deposition (ALD) is a unique technique to design surfaces and interfaces of alkali metal anode at atomic scale with excellent coverage and conformal deposition characteristics under relatively low temperatures with precise control over coating thicknesses.[7] In the reported literature, several types of films have been fabricated as protective layers for both Li and Na metal anodes by ALD, such as metal oxide, polymers, and hybrid films.[8] The ultrathin protective layers by ALD can effectively reduce the dendrite formation and significantly enhance the electrochemical/chemical stability. Although impressive progress has been achieved with ALD-protected alkali metals, challenges remain. First, most of the developed ALD coatings for alkali metals are nonionic conductive and have to be lithiated/sodiated during the electrochemical plating/stripping process. The initial lithiation/sodiation steps may cause the nonhomogeneous Li/Na depositions on the surface of Li/Na metal. The major limitation to deposit ionic conductive layer on Li/Na metal by ALD is the high deposition temperature (above 200 °C) and high precursor temperature (over 180 °C), which is above the melting point of the alkali metals, such as Li (180.5 °C) and Na metals (97.8 °C).[9] Second, although some studies reported the ALD metal oxides for Li or Na protection, the influences of the deposition temperature in the ALD process on the compositions and structures of the coatings have not been investigated in detail. Third, chemical composition and micromechanism of metal oxide and solid-state electrolyte as artificial SEI have not been comprehensively understood.

Herein, we propose a universal approach to fabricate ion-conductive coatings for the alkali metal anodes (Li and Na metal as examples) by ALD. In this process, a two-step strategy is developed to obtain the smooth and stable $LiAlO_x$ or $NaAlO_x$ artificial layer for Li or Na metal anodes by the postlithiation or postsodiation process, respectively. Remarkably, the coating layers are successfully achieved on the surface of metals with excellent quality and significantly improved performances. In addition, we have studied the effects of ALD deposition temperature on the structures of the protective layers and electrochemical performances. The surface and interface chemistry and Li deposition behaviors have been deeply studied by different advanced characteristic techniques. Moreover, the electrochemical phase-field model has been performed to reveal how beneficial the ionic conductive coating is in promoting uniform electrodeposition. On one hand, our design of the ionic conductive protective layer for highly stable alkali metal anodes may open the new window to create conductive layers on Li and Na metal, which can be extended to other ALD materials or other thin film deposition techniques. On the other hand, this study provides new insight into the temperature effects of Li and Na metal as a substrate during the ALD deposition process.

2. Results and Discussion

The ALD metal oxides have been proven to be effective artificial SEI for Li metal anode previously. The deposition temperatures of the reported ALD metal oxides are typically below 150 °C. Two important questions remain in this area. First, is it possible to synthesize the lithiated layers on Li metal by ALD without the introduction of an extra Li precursor? Second, does the ALD deposition temperature affect the structures or compositions of the coatings? To address these questions, we designed the experiments by controlling the ALD deposition temperatures and developed a new two-step strategy. We first studied the ALD deposition temperature effects for Li metal anodes. The ALD Al_2O_3 was used for demonstration because it is the most popular and effective coating for battery interface modification. The deposition temperature of ALD Al_2O_3 was controlled at 120 °C (below the melting point of Li) and 180 °C (close to the melting point of Li), in which the samples are named as Li@nAl_2O_3 and Li@n$LiAlO_x$-in (n = ALD cycles, in =in situ), respectively. For example, the sample with 200 cycles of ALD Al_2O_3 deposited at 120 °C is named as Li@200Al_2O_3 and the sample with 200 cycles of ALD Al_2O_3 deposited at 180 °C is named as Li@200Al_2O_3-in. Furthermore, the two-step approach was developed, as shown in the schematic diagram in **Figure 1**a. In this two-step approach, the ALD Al_2O_3 was first deposited on Li metal at the regular temperature of 120 °C. Then, the ALD chamber was heated up to 180 °C for the post-treatment and kept for half an hour. The samples obtained by this ex situ process are named as Li@n$LiAlO_x$-ex (n = ALD cycles, ex = ex situ). For example, the sample with 200 cycles of ALD Al_2O_3 deposited by the two-step approach is named as Li@200$LiAlO_x$-ex. This approach can be extended to other metal anodes (such as Na metal anode) and other coating layers. For example, the ALD Al_2O_3 is first deposited on the Na metal anode at relatively low temperatures (65 °C) and then post sodiation process is carried out at the temperature close to the melting point of Na metal (97.8 °C).

X-ray photoelectron spectroscopy (XPS) was used to investigate the surface of Li foil after Al_2O_3 deposition under different conditions, which are shown in Figure 1b; and Figures S1–S3 (Supporting Information). From the full spectrum presented in Figures S1–S3 (Supporting Information), peaks around 75 and 532 eV are attributed to Al and O, respectively. It is demonstrated that the Al_2O_3 contained films have been successfully deposited on the Li foils. Figure 1b shows the detailed spectrum of Al 2p for Li@200Al_2O_3 and Li@200$LiAlO_x$-ex. For the Li@200Al_2O_3 deposited at 120 °C, the peak of Al 2p at 75.6 eV represents the typical chemical state with Al_2O_3 reported in the literature.[10] After annealing above the melting point for Li@200$LiAlO_x$-ex, the peak of Al 2p slightly shifts to a lower binding energy of 72.9 eV, indicating the successful reaction and lithiation between Li metal and Al_2O_3 to form the $LiAlO_x$. As shown in Figure S3 (Supporting Information), the peak of Al 2p for Li@$LiAlO_x$-in is also at 72.2 eV, demonstrating the similar $LiAlO_x$ film formed on the Li surface during the high-temperature ALD deposition process. The soft X-ray absorption spectroscopy (XAS) of Near-Edge Structure at Al K edge was carried out to further elaborate on the compositions of the designed samples, as shown in Figure S4 (Supporting Information). For the standard Al_2O_3 powder sample, the main peak at 1564.7 eV is assigned to transitions from the Al 1s orbitals into Al 3p and O 2p antibonding orbitals of t_{1u} symmetry. In the spectra of $LiAlO_2$ powder, this main peak slightly shifts to the low energy of 1563.6 eV. Compared to the Li@200Al_2O_3,

© 2022 Wiley-VCH GmbH

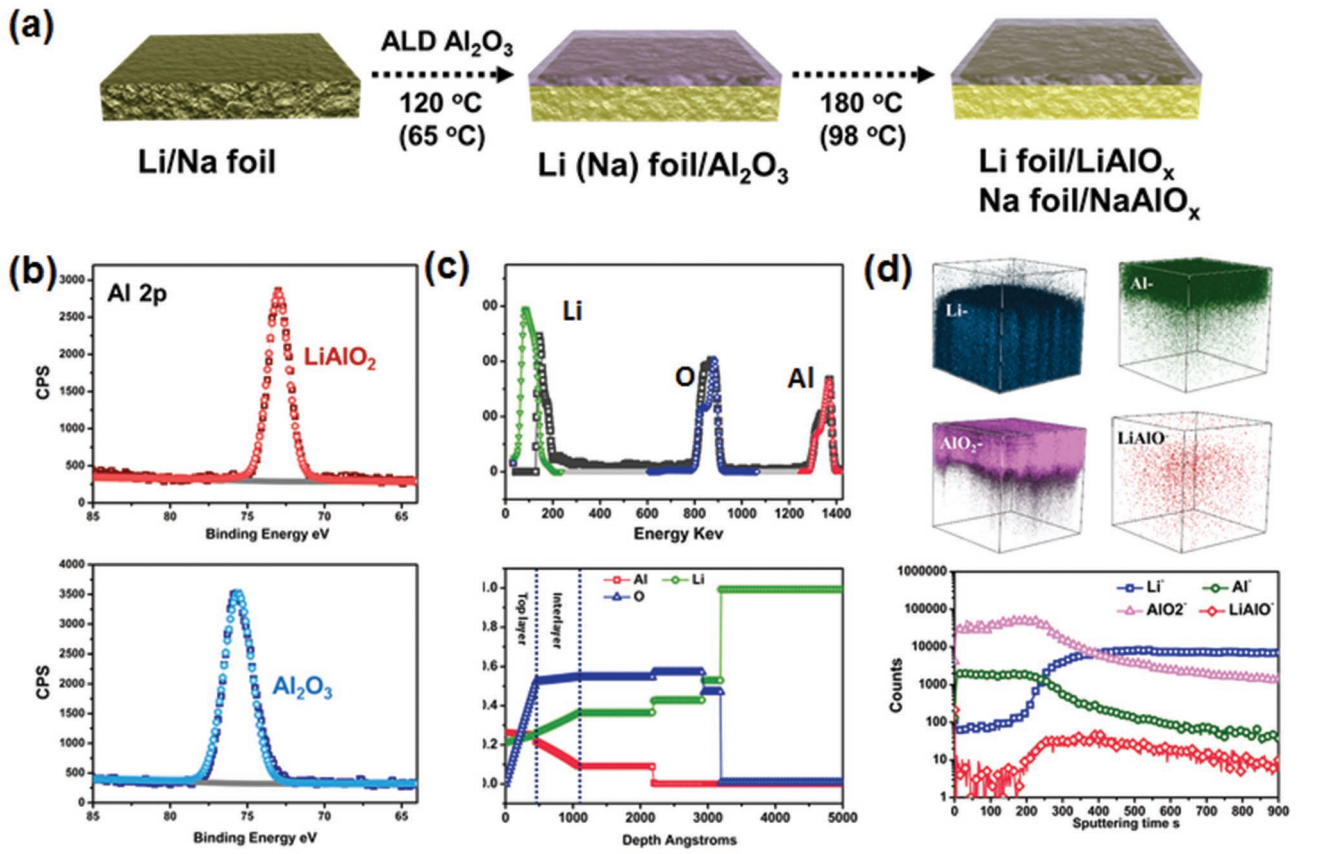

Figure 1. a) Schematic diagram of the two-step strategy to fabricate the ionic conductive layers on Li or Na metal anodes. b) The XPS spectrum of Al 2p of Li@200Al_2O_3 and Li@200$LiAlO_x$-ex. c) The TOF-SIMS secondary ion images, depth profile of various secondary ion species and corresponding 3D images of Li@200$LiAlO_x$-ex. d) The RBS spectra and calculated depth profiles of Li@200$LiAlO_x$-ex.

the pre-edge and main peak features of Li@200$LiAlO_x$-ex and Li@200$LiAlO_x$-in also shift to the lower energy, indicating the lithiation of the films causing the observed change in the local electronic structures of Al. Based on the XPS and XAS results, it can be concluded that both high-temperature ALD and annealing processes can lead to the lithiation of Al_2O_3 to form $LiAlO_x$ on the surface of Li foils. Moreover, the X-ray diffraction (XRD) patterns of Li@200Al_2O_3, Li@200$LiAlO_x$-ex, and Li@200$LiAlO_x$-in are shown in Figure S5 (Supporting Information). From the XRD results, it can be confirmed that all the films on Li metal are amorphous without any peaks related to Al_2O_3 or $LiAlO_2$.

To probe the thicknesses and chemical compositions of the deposited films, time-of-flight secondary ion mass spectrometry (TOF-SIMS) and Rutherford backscattering spectrometry (RBS) were performed, as shown in Figure 1c,d; and Figures S6–S10 (Supporting Information). Figure S6(a) (Supporting Information) presents the RBS spectra and simulated depth profile of Li@200Al_2O_3. Sharp Al and O peaks from the surface can confirm the successful synthesis of an Al-contained layer on Li metal. The thickness of the Al_2O_3 for Li@200Al_2O_3 is about 50 nm with another mixture interlayer of 60 nm. After annealing at 180 °C (Li@200$LiAlO_x$-ex), the top surface layer is still around 50 nm and Li content in the top layer significantly increases due to the lithiation process, further confirming the formation of $LiAlO_x$ (As shown in Figure 1c). Moreover, the Al also diffuses deeper into the Li foil to form the thicker interlayer of another 100 nm. However, the Li@200$LiAlO_x$-in film that was deposited at the melting point of Li displays a much thicker layer of $LiAlO_x$ with a thickness above 230 nm, as shown in Figure S6(b) (Supporting Information). The Al of Li@200$LiAlO_x$-in permeates quite deep into the Li foil with another 200 nm layer. Moreover, the O spectrum of Li@200$LiAlO_x$-in shows that oxygen penetrates above 1 µm on the surface of Li foil. The Li@200$LiAlO_x$-in was fabricated directly at a high temperature at the melting point of Li metal. In this case, the Li is prone to react with H_2O to form the LiOH and this reaction might cause the continuous corrosion of Li metal to form the thick O-rich interlayer. Figure S7 (Supporting Information) shows the RBS spectra and simulated depth profiles of the Li@$LiAlO_x$-ex with different thicknesses (Li@300$LiAlO_x$-ex and Li@500$LiAlO_x$-ex). The thickness increases from ≈80 to ≈100 nm with an increase in ALD cycles from 300 to 500 cycles. From the RBS results, it can be further confirmed that the Li can diffuse and react with Al_2O_3 to form the $LiAlO_x$ for both Li@200$LiAlO_x$-ex and Li@200$LiAlO_x$-in. However, the in-situ high-temperature ALD process causes the corrosion of Li foil with a much thicker O-rich interlayer formation. Based on this, the two-step approach is more promising to form a smooth $LiAlO_x$ with controllable thickness on Li metal anode.

© 2022 Wiley-VCH GmbH

More detailed information is obtained from TOF-SIMS results, as shown in Figure 1d; and Figure S8 (Supporting Information). Figure 1d presents the top surface secondary ion images of Li^-, AlO_2^-, and Al^- and their depth profiles and corresponding 3D reconstructed images for Li@200$LiAlO_x$-ex. From the chemical ion images on the surface of Li, it can be observed that the Li foil is uniformly covered with Al contained films. There is almost no signal of Li^- species detected on the top surface. As expected, the signals of AlO_2^- and Al^- decrease, whereas the signal of Li^- remains constant after 300 s Cs^+ sputtering, which is clearly observed from the depth profiles and corresponding 3D reconstructed images. Moreover, diffusion of Li into the Al-contained films is observed from the 3D reconstructed image, further proving the lithiation of Al_2O_3. However, it needs to be mentioned that the Li^- count is not high because it is the negative ions. Moreover, the interface between the Al-contained layer and Li surface is relatively smooth, indicating that the post-treatment at high temperature does not affect the morphology of the coating layer and Li surface. As a comparison, the depth profiles and corresponding 3D reconstructed images of Li^-, AlO_2^-, LiO^-, and Al^- for Li@200$LiAlO_x$-in are shown in Figure S8 (Supporting Information). Consistent with the RBS result, the in situ high-temperature ALD process on Li metal leads to the very thick Al-contained film (sputtering time over 800 s). Moreover, there is a very strong LiO^- signal from the top surface penetrating to the bulk Li, demonstrating the corrosion of Li metal by the H_2O precursor. Meanwhile, the deposition of the $LiAlO_x$ film is nonuniform and the interface between Li metal and $LiAlO_x$ is quite rough. The surface morphologies of different designs were further tested by scanning electron microscope (SEM), as shown in Figures S9 and S10 (Supporting Information). From the top view SEM images for Li@200$LiAlO_x$-ex, Li@300$LiAlO_x$-ex, and Li@500$LiAlO_x$-ex, the surfaces of the $LiAlO_x$ protected Li foils are relatively smooth and very similar to the pristine Li foil. However, the surfaces of Li@25$LiAlO_x$-in and Li@100$LiAlO_x$-in are quite rough compared to the two-step post-treated samples, which is consistent with the TOF-SIMS analysis.

A similar two-step approach has been applied for Na metal anode to prove the concept and universality. The ALD Al_2O_3 is firstly deposited on the Na metal anode at 65 °C (the sample is named as Na@200Al_2O_3) and then the ALD chamber is heated up at 98 °C for sodiation process (the sample is named as Na@200$NaAlO_x$). Figures S11 and S12 (Supporting Information) show the TOF-SIMS results of surface secondary ion images, depth profile, and corresponding 3D images of secondary ion species for Na@200Al_2O_3 and Na@200$NaAlO_x$, respectively. Compared with Na@200Al_2O_3, the Na is successfully diffused into the Al_2O_3 layer to form the $NaAlO_x$ with the post-sodiation process for Na@200$NaAlO_x$. The stronger signal from Na secondary ion species in the top coating layer is observed from both depth profile and corresponding 3D images for Na@200$NaAlO_x$. The RBS spectra and simulated depth profile of Na@200$NaAlO_x$ are shown in Figure S13 (Supporting Information). The peaks of Al and O from the surface of Na metal further confirm the deposition of Al-based coating on Na metal. With post-treatment at 98 °C, the top $NaAlO_x$ layer is about 40 nm and Na signal is successfully detected in the top layer along with Al-containing coating, which further confirm the formation of $NaAlO_x$. From the SEM images for Na@200Al_2O_3 and Na@200$NaAlO_x$ in Figure S14 (Supporting Information), it can be observed that the surface morphology and structure of the coating layer are not changed with post-sodiation process at melting temperature. The results prove that this two-step approach is universal for fabricating ionic conductive coating layers for alkali metal anodes.

Symmetrical cells were assembled to evaluate the Li plating/stripping behavior of the different designs of the coating layers. Figure S15 (Supporting Information) shows the electrochemical performances of the Li@100Al_2O_3, Li@100$LiAlO_x$-in, and Li@100$LiAlO_x$-ex in the symmetrical cells. At the current density of 1 mA cm^{-2} with the capacity of 1 mAh cm^{-2}, the Li@100Al_2O_3 displays the over-potential of ≈200 mV over 400 h. In the reported literature, the thin Al_2O_3 with few nanometers can improve the cycling performances, however, thick Al_2O_3 may lead to even worse performance due to ionic insulative Al_2O_3 with nonuniform Li deposition (Figure S16, Supporting Information). The Li@100$LiAlO_x$-in deposited at high temperature presents better performances compared to the Li@100Al_2O_3 with the stable over-potential over 600 h. Remarkably, the Li@100$LiAlO_x$-ex shows the best performance of over 800 h among all the samples. After increasing the current density into 5 mA cm^{-2}, the advantage of Li@100$LiAlO_x$-in is not as obvious as at low current density, in which the electrochemical performance of Li@100$LiAlO_x$-in is slightly better than that of the Li@100Al_2O_3. The reason could be that although the Al_2O_3 for Li@100$LiAlO_x$-in was lithiated under the high-temperature ALD, the continuous corrosion of Li metal by H_2O lead to the O-rich interlayer and nonuniform $LiAlO_x$ layer with a rough surface. Promisingly, the Li@100$LiAlO_x$-ex keeps the superiority compared with the other two designs. In this case, it can be concluded that the two-step approach (Li@n$LiAlO_x$-ex) with a post-treatment can be considered as an effective approach to lithiate the Al_2O_3 to form $LiAlO_x$ on the Li metal surface with high uniformity and controlled thicknesses. In addition, the thickness of Li@n$LiAlO_x$-ex was further optimized, as shown in Figure S16 (Supporting Information). Various thicknesses of 50, 100, 150, 300, and 500 cycles of $LiAlO_x$ were deposited on the Li anodes. At different current densities (1 and 3 mA cm^{-2}), the optimized thickness of the $LiAlO_x$ is around 150–300 ALD cycles.

As discussed above, the two-step approach with post-treatment produces high quality and preciously controlled $LiAlO_x$ coating on the Li surface. In this case, we picked up the Li@200$LiAlO_x$-ex as an example of the battery performance study. **Figure 2**a; and Figure S17(a) (Supporting Information) show the cycling stability of bare Li foil and Li@200$LiAlO_x$-ex at different conditions using conventional Li foil with a thickness of 350 µm. At the current density of 1 mA cm^{-2} with the capacity of 1 mAh cm^{-2} (Figure S17, Supporting Information), the initial Li stripping/plating over-potential of bare Li foil is ≈50 mV (vs Li^+/Li) and rapidly increases to over 200 mV (vs Li^+/Li) after ≈650 h. Then, the overpotential of bare Li foil keeps over 300 mV and is fluctuant. In contrast, Li@200$LiAlO_x$-ex displays significant improvement in cycling stability. The overpotential of Li@200$LiAlO_x$-ex is stable with a low overpotential of 100 mV after 1000 h without any short circuit. Figure 2a displays the symmetrical cell performances of bare Li foil and

© 2022 Wiley-VCH GmbH

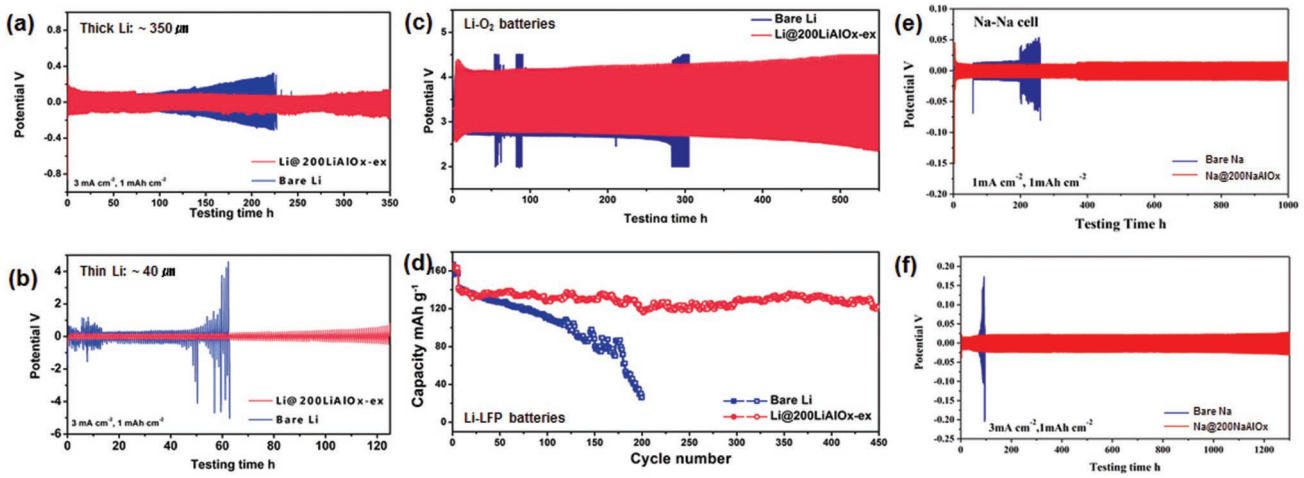

Figure 2. The overpotential of Li/Li symmetric cells using bare Li foil and Li@200LiAlO$_x$-ex in the carbonate-based electrolyte at the current density of 3 mA cm^{-2} with the capacity of 1 mAh cm^{-2} with a) thick Li foil (≈350 µm) and b) thin Li foil (≈40 µm). c) Cycling performances of Li-O$_2$ full cells (CP-NCNTs as the cathode) using bare Li foil and Li@200LiAlO$_x$-ex as anode electrode at the current density of 0.1 mA cm^{-2}. d) Cycling performances of full cells (C/LiFePO$_4$ as the cathode) using bare Li foil and Li@200LiAlO$_x$-ex as anode electrode at 1 C (1 C = 170 mA g^{-1}). The overpotential of Na/Na symmetric cells using bare Na foil and Na@200NaAlO$_x$ under the conditions of e) 1 mA cm^{-2}/1 mAh cm^{-2} and f) 3 mA cm^{-2}/1 mAh cm^{-2}.

Li@200LiAlO$_x$-ex at a higher current density of 3 mA cm^{-2}. The bare Li foil still shows the increased overpotential and subsequently short-circuited after ≈225 h. In comparison, the Li@200LiAlO$_x$-ex displays improved stability with a stable overpotential over 350 h. For more practical applications, thin Li foil is requested to obtain high energy density. In this case, we also used the thin Li foil with a thickness of 40 µm. The electrochemical performances of the symmetrical cell for the bare Li foil and Li@200LiAlO$_x$-ex using thin Li foil are shown in Figure 2b; and Figure S17(b) (Supporting Information). In Figure S17(b) (Supporting Information), the overpotential of the bare thin Li foil started to increase after 200 h and reached 1000 mV after 225 h, indicating the depletion of the Li metal and formation of dead Li layers. As a comparison, the thin Li@200LiAlO$_x$-ex is stable over ≈330 h without any short circuit. The bare thin Li foil is extremely unstable at the high current density of 3 mA cm^{-2}, as shown in Figure 2b. The lifetime of the bare thin Li foil is less than 50 h. However, the cycling stability of the thin Li@200LiAlO$_x$-ex is over 120 h and about two times higher than that of the thin Li foil. It is also worth mentioning that the electrochemical performances of the thin Li even with coatings are generally worse than the thick Li due to the consumption of Li metal and electrolyte, which has been widely recognized in this field.

In order to further demonstrate the unique properties of the LiAlO$_x$ coating, different full cell systems have been investigated using bare Li foil and Li@LiAlO$_x$-ex electrodes as the anode. Based on the symmetric cell performances discussed above, the Li@200LiAlO$_x$-ex electrode is used as an example for the full cells. The electrochemical performances of the Li–O$_2$ batteries were performed by using 2016-type coin cells of a carbon-based cathode (N-doped carbon nanotube grown on carbon paper, NCNTs-CP), an electrolyte of LiClO$_4$ in tetraethylene glycol dimethyl ether (TEGDME) and a bare Li foil or protected Li foil (Li@200LiAlO$_x$-ex) as the anodes. Figure 2c; and Figure S18 (Supporting Information) present the charge–discharge profiles and cycling performances of the Li–O$_2$ cells using bare Li foil and Li@200LiAlO$_x$-ex as anodes, respectively. For the bare Li anode, the performance of the Li–O$_2$ cell is less than 280 h (140 cycles). However, the protected Li of Li@200LiAlO$_x$-ex delivers a significantly improved cycling stability of ≈550 h (300 cycles), which is approximately two times of the cell using a bare Li anode. The results reveal that the LiAlO$_x$ coating can effectively mitigate the degradation of Li anodes against O$_2$ corrosion and Li dendrite formation. Furthermore, the Li-LiFePO$_4$ (LFP) batteries were demonstrated in Figure 2d. The LFP cells were first activated at 0.1 C for 5 cycles and then cycled at 1 C for long-term cycling performance. In the cell using bare Li foil, the discharge/charge capacity starts fading after 100 cycles and decreases to about 30 mAh g^{-1} after 200 cycles. However, using Li@200LiAlO$_x$-ex as the anode, the cell maintains an extremely stable capacity of ≈120 mAh g^{-1} after 450 cycles.

To further prove the concept, the Na–Na symmetrical cells were assembled to evaluate the Na plating/stripping behavior. Figure 2e presents the electrochemical performances of the bare Na foil and Na@200NaAlO$_x$ in the symmetrical cells under the condition of 1 mA cm^{-2}/1 mAh cm^{-2}. The initial overpotential of bare Na foil is ≈20 mV (vs Na$^+$/Na) and rapidly increases to over 40 mV (vs Na$^+$/Na) after ≈200 h. After about 280 h, a sudden drop of the overpotential is observed, indicating the short circuit occurs for the bare Na. Very promisingly, for the Na@200NaAlO$_x$, the cell demonstrates stable performance for over 1000 h with a low overpotential of 20 mV. When the current density was increased to 3 mA cm^{-2}, the overpotential of the bare Na increased dramatically up to 150 mV after only 100 h and a short circuit occurred shortly thereafter, as shown in Figure 2f. For the Na@200NaAlO$_x$, even at a higher current density of 3 mA cm^{-2}, the overpotential is extremely stable over 1200 h without any short circuit. The electrochemical performances for both Li and Na metal anodes demonstrate that the LiAlO$_x$/NaAlO$_x$ coating can effectively improve the stability of Li/Na metal anode in different systems and shows potential

© 2022 Wiley-VCH GmbH

for use in next-generation Li/Na-metal batteries. Particularly, $LiAlO_x$ coating derived from the two-step process demonstrates unique properties and superior performances compared to the Al_2O_3 and $LiAlO_x$ deposited directly at high temperatures. This further proves that this approach is universal to be extended to different alkali metal anodes.

To understand the influence of the $LiAlO_x$ layers on the Li deposition behavior, the morphology of Li metal was imaged by SEM after cycling. Figure S19 (Supporting Information) shows the SEM images of pristine Li foil after the different depths of electrochemical cycling (10, 20, and 30 cycles) at a current density of 1 mA cm^{-2} with a capacity limit of 1 mAh cm^{-2}. The mossy Li and dead Li layers are formed within 10 cycles, becoming more serious after deeper cycling. With 50 cycles of Li plating/stripping (**Figure 3**a), a porous mossy structure with a rougher surface and obvious cracks are observed on the Li. These issues cause the increasing polarization of the cell and finally lead to short circuit. In comparison, the morphologies of the Li@200$LiAlO_x$-ex are drastically different, as shown in Figure S19 (Supporting Information) and Figure 3a. With the different cycling stages (10, 20, and 30 cycles), as shown in Figure S20 (Supporting Information), no visible morphological change can be observed from the surfaces of the Li@200$LiAlO_x$-ex. After 50 cycles of Li plating/stripping, the Li dendrite growth, and dead Li formation are effectively reduced with the $LiAlO_x$ coating, which leads to significantly enhanced electrochemical performances.

Besides the morphology, the chemical composition of the SEI is another critical factor for the Li deposition behavior and electrochemical performances. To understand the compositional changes following the plating/stripping cycling experiments, TOF-SIMS measurements were carried out. Figure S21 (Supporting Information) presents the TOF-SIMS results (including surface chemical ion images, depth profiles, and corresponding 3D reconstructed images) of bare Li foil after plating/stripping cycling experiments at a current density of 1 mA cm^{-2} with a capacity limit of 1 mAh cm^{-2}. The bare Li shows significant penetration of F from electrolyte with a long sputtering time (over 500 s), which is related to the thick dead Li layer formation. However, as shown in Figure 3b; and Figure S22 (Supporting Information), the $LiAlO_x$ coating remains on the top surface and with only slight changes compared with the spectra before cycling, in which the sputtering time is around 400 s. From the TOF-SIMS analysis of the SEI, it is found that the $LiAlO_x$ coating is robust and chemical/electrochemical stable during the Li plating/stripping process. To have a better

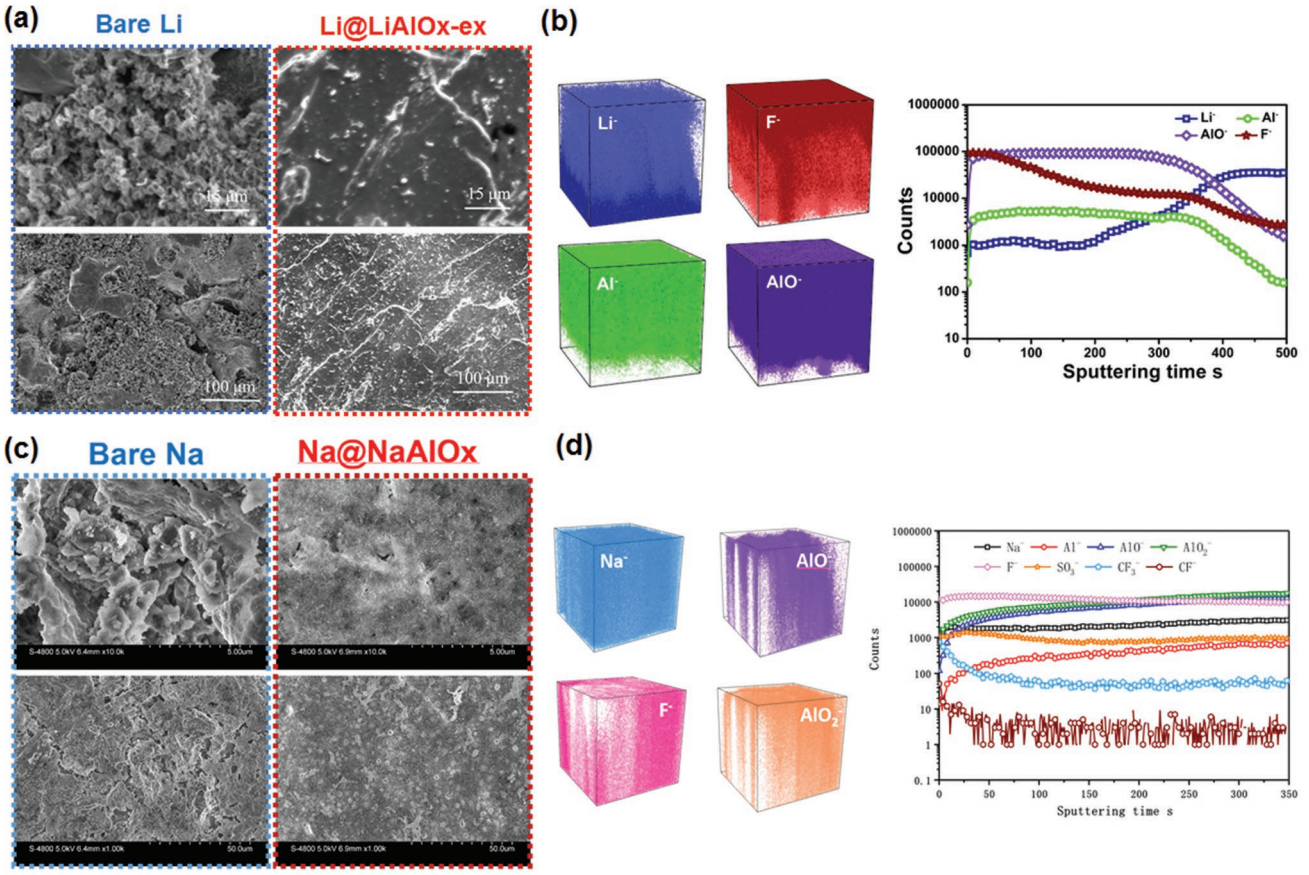

Figure 3. Top-view SEM images of a) bare Li foil and Li@200$LiAlO_x$-ex after electrochemical cycling (50 cycles). b) The TOF-SIMS depth profiles and corresponding 3D reconstructed images of Li@200$LiAlO_x$-ex after electrochemical cycling. Top-view SEM images of c) bare Na foil and Na@200$NaAlO_x$ after electrochemical cycling (50 cycles). d) The TOF-SIMS depth profiles and corresponding 3D reconstructed images of Na@200$NaAlO_x$ after electrochemical cycling.

© 2022 Wiley-VCH GmbH

understanding and comparison of the SEI, the XAS at Al K-edge was performed for Li@200Al_2O_3, Li@200$LiAlO_x$-in, and Li@200$LiAlO_x$-ex after cycling. After cycling, the XAS spectra of Al K-edge (Figure S23, Supporting Information) become broader, with the peak shifts to higher energy compared to that of before cycling. Moreover, the intensities of spectra for Li@200Al_2O_3 and Li@200$LiAlO_x$-in dramatically decrease compared to that of Li@200$LiAlO_x$-ex, indicating the degradation of the coating layers during cycling. It further confirms that Li@200$LiAlO_x$-ex is the most stable protective layer during cycling.

Similarly, the surface morphology and composition of bare Na and Na@200$NaAlO_x$ after electrochemical cycling were further investigated. Figure 3c shows the top-view SEM images of bare Na and Na@200$NaAlO_x$ after cycling. For the bare Na, the mossy Na is formed after the cycling, and the surface of the Na becomes rough with cracks. Remarkably, the surface of the Na@200$NaAlO_x$ after cycling is much smoother without any dendritic and mossy Na formation, which is one of the reasons for the significantly enhanced electrochemical performances. The chemical composition of the interface was studied by TOF-SIMS, as shown in Figure S24 (Supporting Information); and Figure 3d. For the bare Na after cycling, strong signals of F^-, CF_3^-, SO_3^- secondary ion species are observed, demonstrating the decomposition of the electrolyte components as well as the thick dead Na layer growth. As a comparison, the AlO^- and AlO_2^- secondary ion species from the $NaAlO_x$ layer remain with minor changes, indicating that the $NaAlO_x$ protective layer is extremely stable during the electrochemical cycling, consistent with the results of electrochemical performances. The RBS spectra and simulated depth profile of Na@200$NaAlO_x$ after cycling are shown in Figure S25 (Supporting Information). From the RBS depth profile, it can be confirmed that the thickness of the $NaAlO_x$ layer remains as 40 nm as the top layer, further indicating the robust behavior of the $NaAlO_x$ during electrochemical cycling.

To confirm the benefit of highly ionic conductive coating layer, the electrochemical phase-field model was performed. The approximated Li-ion diffusion coefficient of each coating used in this study are as follows: $LiAlO_x$ (1.4×10^{-11} m^2 s^{-1}) >> uncoated surface (4.6×10^{-13} m^2 s^{-1}) > Al_2O_3 (1.0×10^{-13} m^2 s^{-1}).[11] **Figure 4**a–c illustrates the simulated spatiotemporal evolution of deposits Li and the associated Li-ion distribution during Li plating under different coating conditions. Despite the same initial surface morphology for all studies, in which two small Li perturbations are introduced, Li@$LiAlO_x$ shows the surface of deposited Li remains uniform throughout the Li plating process, which is consistent with the experimental characterization that no dendrite after cycling is observed under the $LiAlO_x$ coating (Figure 3a; or Figure S19, Supporting Information). This

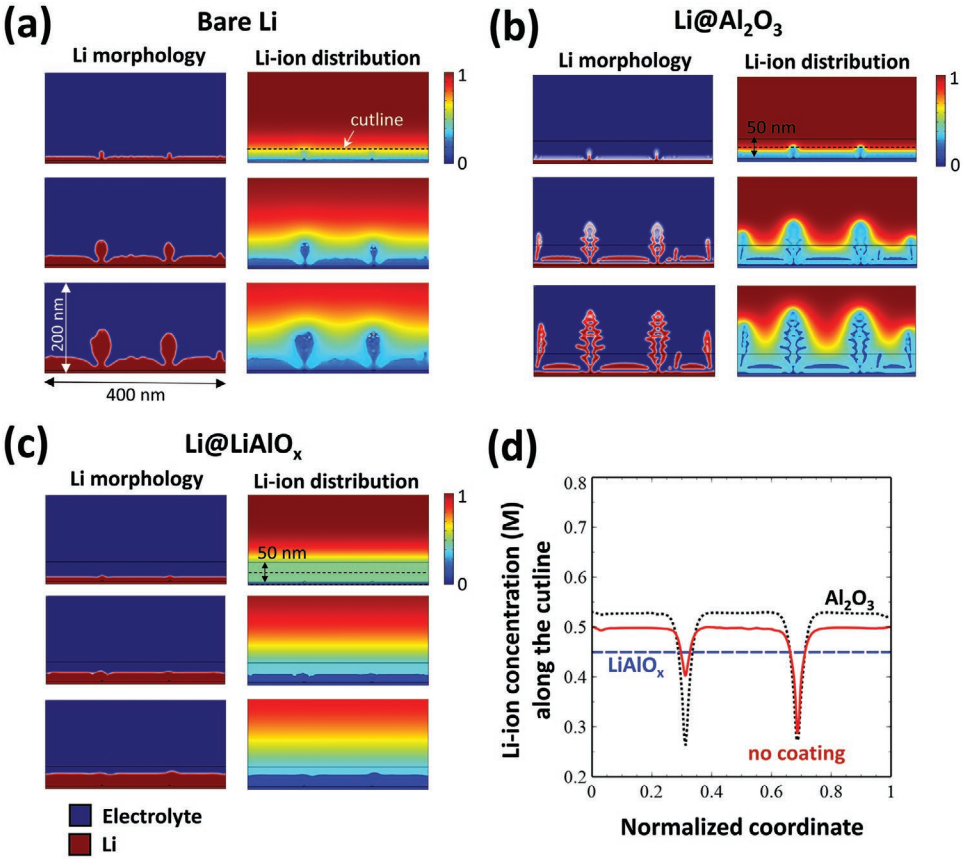

Figure 4. The simulated spatiotemporal evolution of the morphological for deposits Li and the distribution of Li-ion concentration under different coatings: a) bare Li, b) Li@Al_2O_3, and c) Li@$LiAlO_x$. d) The plot of Li-ion concentration near the interface at the beginning of the Li deposition process, showing the high ionic diffusivity layer is beneficial for homogenizing the Li-ion distribution, which is a key driving force for uniform Li deposition.

© 2022 Wiley-VCH GmbH

is thanks to the intrinsic nature of the highly ionic conductive layer. Once Li ions are reduced to Li atoms by the charge transfer reaction at the electrode surface, Li ions in the coating layer (or electrolyte) quickly diffuse to the interface to replace the depleted Li ions. Thus, the homogeneous distribution of Li ions along the interface is well-maintained. On the other hand, when Li-ion diffusion near the interface is slow, bare Li as an example, the gradient of Li-ion concentration closed to the interface is evident, as shown in Figure 4d. The variation of Li-ion concentration along the interface contributes to the nonuniform driving force for Li electrodeposition, thus resulting in the dendritic morphology of Li. The results agree with the experimental observation in Figure 3a; or Figure S18 (Supporting Information), showing porous mossy Li structure after cycling. Moreover, for Li@Al_2O_3, whose coating layer is considered thick and highly nonionic conductive, the Li dendrite quickly grows due to the significant Li-ion concentration gradient, substantially deteriorating cyclic performance (Figure S14, Supporting Information).

3. Conclusion

In conclusion, we successfully developed a universal approach to deposit ionic conductive interfaces for the alkali metal anodes by ALD. In the unique two-step ALD process, there is no Li/Na precursor required during deposition and Li/Na metal plays the role of Li/Na source. The $LiAlO_x$/$NaAlO_x$ coatings derived by a two-step strategy are uniform, smooth, and highly controllable. The ionic conductive coating layers can significantly improve the electrochemical performances of the Li and Na metal anodes in symmetric cells and full cells. Multiple evidence reveals that the ionic conductive coatings are chemically and electrochemically stable during electrochemical plating/stripping and can reduce the Li/Na dendrite growth and dead Li/Na layer formation, resulting in performance improvement. We further investigated the influence of the ALD deposition temperatures on the Li metal anode's morphology, composition, and performance. Although the $LiAlO_x$ is also directly achieved with a high-temperature ALD process (Li@n$LiAlO_x$-in), the surface of Li metal turns rough and corroded when the deposition temperature is above the melting point. We believe that this work not only opens a new window on creating ionic conductive layers on alkali metal without alkali precursor, but also provides new insight into the temperature effects during the ALD deposition process when using temperature-sensitive alkali metal as a substrate.

Supporting Information

Supporting Information is available from the Wiley Online Library or from the author.

Acknowledgements

E.J. and K.T. contributed equally to this work. This research was supported by the Natural Science and Engineering Research Council of Canada (NSERC), the Canada Foundation for Innovation (CFI), and the University of Western Ontario (UWO). The authors gratefully acknowledge Dr. Heng-Yong Nie for his help in the discussion on TOF-SIMS results. They would like to acknowledge the technical expertise of Jack Hendriks at the Western Tandetron Accelerator Facility. This research used resources of the Advanced Light Source, a DOE Office of Science User Facility under Contract No. DE-AC02-05CH11231.

Conflict of Interest

The authors declare no conflict of interest.

Data Availability Statement

The data that support the findings of this study are available from the corresponding author upon reasonable request.

Keywords

alkali metal anodes, atomic layer deposition, interface engineering, next generation batteries

Received: May 16, 2022
Revised: June 23, 2022
Published online:

[1] a) X. B. Cheng, R. Zhang, C. Z. Zhao, Q. Zhang, *Chem. Rev.* **2017**, *117*, 10403; b) D. Lin, Y. Liu, Y. Cui, *Nat. Nanotechnol.* **2017**, *12*, 194; c) Y. Zhao, K. R. Adair, X. Sun, *Energy Environ. Sci.* **2018**, *11*, 2673; d) S. Lou, F. Zhang, C. Fu, M. Chen, Y. Ma, G. Yin, J. Wang, *Adv. Mater.* **2021**, *33*, 2000721. e) Y.-J. Lei, Z.-C. Yan, W.-H. Lai, S.-L. Chou, Y.-X. Wang, H.-K. Liu, S.-X. Dou, *Electrochem. Energy Rev.* **2020**, *3*, 766.

[2] a) H. Wang, Y. Liu, Y. Li, Y. Cui, *Electrochem. Energy Rev.* **2019**, *2*, 509; b) X. Zhang, Y. Yang, Z. Zhou, *Chem. Soc. Rev.* **2020**, *49*, 3040.

[3] a) R. Xu, X.-B. Cheng, C. Yan, X.-Q. Zhang, Y. Xiao, C.-Z. Zhao, J.-Q. Huang, Q. Zhang, *Matter* **2019**, *1*, 317; b) Z. Luo, X. Qiu, C. Liu, S. Li, C. Wang, G. Zou, H. Hou, X. Ji, *Nano Energy* **2021**, *79*, 105507.

[4] a) Z. Han, C. Zhang, Q. Lin, Y. Zhang, Y. Deng, J. Han, D. Wu, F. Kang, Q. H. Yang, W. Lv, *Small Methods* **2021**, *5*, 2001035; b) Y. Chu, Y. Shen, F. Guo, X. Zhao, Q. Dong, Q. Zhang, W. Li, H. Chen, Z. Luo, L. Chen, *Electrochem. Energy Rev.* **2019**, *3*, 187.

[5] a) G. Wang, C. Chen, Y. Chen, X. Kang, C. Yang, F. Wang, Y. Liu, X. Xiong, *Angew. Chem., Int. Ed. Engl.* **2020**, *59*, 2055; b) D. H. Liu, Z. Bai, M. Li, A. Yu, D. Luo, W. Liu, L. Yang, J. Lu, K. Amine, Z. Chen, *Chem. Soc. Rev.* **2020**, *49*, 5407.

[6] a) Y. Gao, Z. Yan, J. L. Gray, X. He, D. Wang, T. Chen, Q. Huang, Y. C. Li, H. Wang, S. H. Kim, T. E. Mallouk, D. Wang, *Nat. Mater.* **2019**, *18*, 384; b) Y. Gao, T. Rojas, K. Wang, S. Liu, D. Wang, T. Chen, H. Wang, A. T. Ngo, D. Wang, *Nat. Energy* **2020**, *5*, 534; c) J. Xie, L. Liao, Y. Gong, Y. Li, F. Shi, A. Pei, J. Sun, R. Zhang, B. Kong, R. Subbaraman, J. Christensen, Y. Cui, *Sci. Adv.* **2017**, *3*, eaao3170; d) J. Wu, Z. Rao, X. Liu, Y. Shen, C. Fang, L. Yuan, Z. Li, W. Zhang, X. Xie, Y. Huang, *Adv. Mater.* **2021**, *33*, 2007428; e) X.-D. Lin, Y. Gu, X.-R. Shen, W.-W. Wang, Y.-H. Hong, Q.-H. Wu, Z.-Y. Zhou, D.-Y. Wu, J.-K. Chang, M.-S. Zheng, B.-W. Mao, Q.-F. Dong, *Energy Environ. Sci.* **2021**, *14*, 1439; f) J. Xiao, P. Zhai, Y. Wei, X. Zhang, W. Yang, S. Cui, C. Jin, W. Liu, X. Wang, H. Jiang, Z. Luo, X. Zhang, Y. Gong, *Nano Lett.* **2020**, *20*, 3911.

[7] a) Y. Zhao, L. Zhang, J. Liu, K. Adair, F. Zhao, Y. Sun, T. Wu, X. Bi, K. Amine, J. Lu, X. Sun, *Chem. Soc. Rev.* **2021**, *50*, 3889; b) Y. Zhao, K. Zheng, X. Sun, *Joule* **2018**, *2*, 2583.

 © 2022 Wiley-VCH GmbH

[8] a) R. Zhang, Y. Li, L. Qiao, D. Li, J. Deng, J. Zhou, L. Xie, Y. Hou, T. Wang, W. Tian, J. Cao, F. Cheng, B. Yang, K. Liang, P. Chen, B. Kong, *Energy Storage Mater.* **2021**, *37*, 123; b) Y. Sun, C. Zhao, K. R. Adair, Y. Zhao, L. V. Goncharova, J. Liang, C. Wang, J. Li, R. Li, M. Cai, T.-K. Sham, X. Sun, *Energy Environ. Sci.* **2021**, *14*, 4085; c) S. T. Oyakhire, W. Huang, H. Wang, D. T. Boyle, J. R. Schneider, C. Paula, Y. Wu, Y. Cui, S. F. Bent, *Adv. Energy Mater.* **2020**, *10*, 2002736; d) Y. Sun, M. Amirmaleki, Y. Zhao, C. Zhao, J. Liang, C. Wang, K. R. Adair, J. Li, T. Cui, G. Wang, R. Li, T. Filleter, M. Cai, T. K. Sham, X. Sun, *Adv. Energy Mater.* **2020**, *10*, 2001139; e) Y. Zhao, L. V. Goncharova, A. Lushington, Q. Sun, H. Yadegari, B. Wang, W. Xiao, R. Li, X. Sun, *Adv. Mater.* **2017**, *29*, 1606663; f) Y. Zhao, L. V. Goncharova, Q. Zhang, P. Kaghazchi, Q. Sun, A. Lushington, B. Wang, R. Li, X. Sun, *Nano Lett.* **2017**, *17*, 5653; g) S. Zhang, Y. Zhao, F. Zhao, L. Zhang, C. Wang, X. Li, J. Liang, W. Li, Q. Sun, C. Yu, J. Luo, K. Doyle-Davis, R. Li, T. K. Sham, X. Sun, *Adv. Funct. Mater.* **2020**, *30*, 2001118.

[9] a) J. Liu, M. N. Banis, B. Xiao, Q. Sun, A. Lushington, R. Li, J. Guo, T.-K. Sham, X. Sun, *J. Mater. Chem. A* **2015**, *3*, 24281; b) B. Wang, Y. Zhao, M. N. Banis, Q. Sun, K. R. Adair, R. Li, T. K. Sham, X. Sun, *ACS Appl. Mater. Interfaces* **2018**, *10*, 1654.

[10] L. Cheng, X. Qin, A. T. Lucero, A. Azcatl, J. Huang, R. M. Wallace, K. Cho, J. Kim, *ACS Appl. Mater. Interfaces* **2014**, *6*, 11834.

[11] a) B. Huang, Z. Zhao, Y. Sun, M. Wang, L. Chen, Y. Gu, *Solid State Ion* **2019**, *338*, 31; b) S. C. Jung, H. J. Kim, J. W. Choi, Y. K. Han, *Nano Lett.* **2014**, *14*, 6559.

© 2022 Wiley-VCH GmbH